EDGE ARTICLE

Temperature-driven reaction pathways in alkane direct dehydrogenation over metal-free nitrogen doped carbocatalysts

Jie Zhang, [†](ab) Ranjan K. Behera,[†b] Vy T. Nguyen,[†c] Zhenhao Liu, [b]
Juan D. Jimenez, [d] Kasala Prabhakar Reddy,[d] Jorge Moncada, [ef]
Cherno Jaye, [e] Jinsu Oh, [a] Chao Meng, [ab] Lin Zhou,[ab]
Sanjaya D. Senanayake, [d] Bin Wang, [*c] Long Qi [*ab] and Wenyu Huang [*ab]

Metal-free heteroatom-doped carbocatalysts are promising alternatives to precious metals for alkane direct dehydrogenation/hydrogenation and reversible hydrogen storage, yet the nature of their active sites remains poorly understood. This study investigates a nitrogen assembly carbocatalyst (NAC) for efficient and selective hydrocarbon dehydrogenation. For ethylbenzene, NAC maintains a selectivity of >99% towards styrene at a conversion of >20% for 120 hours at a weight hourly space velocity of 0.4 h^{-1}. Theoretical studies suggest that closely spaced graphitic nitrogen sites are the active sites for the chemisorption and dehydrogenation of ethylbenzene, and the robustness of these sites is supported by ambient-pressure X-ray photoelectron spectroscopy. Kinetic analysis reveals a temperature-dependent reaction profile, with distinct activation energies and reaction orders at 300 and 500 °C. Isotope-labeling studies indicate that dehydrogenation primarily proceeds *via* initial cleavage of the benzylic C−H bond, and the faster desorption of ethylbenzene at higher temperatures contributes to the difference in kinetic behavior. Importantly, the NAC catalyst also enables efficient hydrogenation of styrene back to ethylbenzene at 250 °C, allowing for reversible hydrogen storage using a single catalyst at moderate temperatures. These findings underscore the significance of constructing high densities of closely spaced graphitic nitrogen in carbocatalysts for enhanced activity and selectivity.

Introduction

Direct dehydrogenation (DDH) of alkanes is a vital process for producing commodity chemicals (olefins, aromatics, and hydrogen).[1] In particular, the DDH of propane and ethane is highly desirable with the surging supply of shale gas.[2] DDH is also a key transformation for reversible hydrogen storage using liquid organic hydrogen carriers (LOHCs), such as methyl-cyclohexane.[3] The liquid nature and chemical stability of LOHCs at ambient conditions make them unique and desirable for long-term storage, long-range transportation, and global trading, in contrast to compressed or liquefied hydrogen.

The acceptorless DDH of alkanes typically requires high temperatures and thus significant energy input to achieve satisfactory conversions. Transition metal-based catalysts, especially those containing precious metals, are commonly used in catalytic DDH reactions,[4,5] but metal sintering and coking are frequently encountered (typically at 400 to 700 °C).[6–9] In addition, very few reports used the same catalysts to achieve reversible hydrogen storage for dehydrogenation and rehydrogenation.[10] Therefore, developing alternative catalysts for DDH and reverse reactions with higher stability and activity is critical to advancing efficient hydrocarbon transformation and reducing energy consumption.

Recently, metal-free carbon-based catalysts, including nanodiamonds, activated carbon, carbon nanotubes, or heteroatom-doped carbon materials, have been widely studied for DDH reactions of alkanes and oxygenates.[11–13] For example, the nanodiamond catalyst exhibits high activity for ethyl-benzene DDH reaction with a styrene yield of 40% at 550 °C, higher than that of the commercial potassium-promoted Fe_2O_3 catalyst.[14] The oxygen-containing functional groups (*e.g.*, ketone, lactone, *etc.*) on the carbon surface have been proposed as the active sites for alkane activation.[15] Besides oxygen species, doping with heteroatoms (in particular nitrogen) also

aU.S. DOE Ames National Laboratory, Ames, IA, 50011, USA. E-mail: lqi@iastate.edu; whuang@iastate.edu

bDepartment of Chemistry, Iowa State University, Ames, Iowa 50011, USA

cSchool of Sustainable Chemical, Biological and Materials Engineering, University of Oklahoma, Norman, OK 73019, USA. E-mail: wang_cbme@ou.edu

dChemistry Division, Brookhaven National Laboratory, Upton, NY, 11973, USA

eMaterial Measurement Laboratory, National Institute of Standards and Technology, Gaithersburg, MD 20899, USA

fNational Synchrotron Light Source II, Brookhaven National Laboratory, Upton, New York 11973, USA

† These authors contributed equally to this work.

enhances catalytic activity for non-oxidative alkane dehydrogenation.[16–18]

In our previous work, nitrogen assembly carbocatalysts (NACs) exhibited outstanding DDH activity toward various molecules containing N-heterocycles, and full dehydrogenation products can be achieved even at room temperature.[18] The closely spaced graphitic nitrogen atoms (or graphitic nitrogen assembly) were proposed as the most plausible active sites for DDH; however, the lack of suitable characterization techniques makes it difficult to decipher the DDH reaction mechanism and pathway on NAC catalysts at the atomic level. Herein, we investigated the NAC catalyst for the gas-phase dehydrogenation of four hydrocarbon substrates. The NAC catalyst exhibits high and stable dehydrogenation activity, allowing for detailed kinetic, spectroscopic, and mechanistic interrogation to elucidate the active site structures and surface reactions. Kinetic studies and isotope-labeling experiments reveal distinct temperature-dependent reaction pathways, resulting from the different reactivities of surface chemisorbed intermediates, as supported by theoretical studies. The same catalyst can effectively transform styrene back into ethylbenzene at 250 °C, which lays the foundation for efficient and reversible hydrogen storage and release using a single catalyst under mild conditions.

Results and discussion

Synthesis and characterization

The nitrogen-assembly carbon (NAC) catalyst was synthesized utilizing a hard templating method.[18–20] As illustrated in Fig. 1a, ethylenediamine and carbon tetrachloride were cross-polymerized in the mesopores of SBA-15 silica (a surface area of ≈ 780 m^2 g^{-1} and a pore diameter of ≈ 7.5 nm, Fig. S1). The resulting mixture was then pyrolyzed at 800 °C under flowing argon, followed by silica etching to obtain the carbon catalyst. The wide-angle powder X-ray diffraction (XRD) patterns showed only two broad peaks, centered at 25° and 43° (Fig. S2), which were assigned to diffraction from the (002) and (004) planes of the graphitic carbon, respectively.[21] Transmission electron microscopy (TEM) images of the NAC catalyst are presented in Fig. 1b, c and S3. Low-magnification TEM images reveal that the catalyst exhibits ordered parallel mesopores (Fig. S3), corroborated by the high surface area of the NAC materials (670 m^2 g^{-1}) measured by the N_2 physisorption (Fig. S4). In addition, high-magnification TEM images reveal that the catalyst features parallel mesoporous channels with a periodicity of 8.2 nm (Fig. 1c).

High-angle annular dark field (HAADF) imaging using an aberration-corrected scanning transmission electron microscopy (STEM) combined with electron energy loss spectroscopy (EELS) was used to investigate the distribution and coordination environment of elements. The EELS spectrum (Fig. S5) displays two types of carbon K-edge peaks: (1) 1s → π* transition at 285 eV and (2) 1s → σ* transition at 290 eV. Additionally, two peaks between 396 eV and 421 eV indicate the presence of nitrogen atoms. No significant energy loss between 520 and 560 eV, indicating the amount of oxygen species, which are frequently viewed as active sites in carbocatalysts for direct

dehydrogenation reactions, is below the detection limit.[22] The homogeneous spatial distributions of carbon and nitrogen elements in the NAC catalyst were visualized by EELS mapping based on the intensity variation of their energy loss peaks (Fig. S6a) and energy dispersive spectroscopy (EDS) mapping of the NAC catalyst (Fig. 1d–g).

Near-edge X-ray absorption fine structure (NEXAFS) spectroscopy (Fig. 1h) has been applied to determine the chemical environment of the NAC catalyst. N K-edge NEXAFS spectra illustrate that the N atoms are incorporated into the graphene lattice as pyridinic and graphitic Ns, with peaks at approximately 398.5 eV and 401.2 eV, respectively. Another pronounced π*-resonances at 399.9 eV is attributed to pyrrolic N. The oxidized nitrogen species could be responsible for a shoulder at the high-energy side of the peak (≈ 403.0 eV).[23] The peak at ≈ 408.0 eV is assigned to the σ* C–N–C or C–N bonds.[12] The signals were collected in partial electron yield (PEY) and total electron yield (TEY) detection modes, which are surface- and bulk-sensitive, respectively.[24] The fact that PEY and TEY spectra are nearly identical further confirms that all N and C species are distributed evenly in the bulk and surface of the material.

Furthermore, the quantities of individual carbon and nitrogen species in the NAC catalyst can be assessed by X-ray photoelectron spectroscopy (XPS). The total carbon and nitrogen content of the NAC catalyst is 91 and 9 at%, respectively, equivalent to a C/N ratio of 10.3. Based on the results of N K-edge NEXAFS, the N 1s XPS peak can be deconvoluted into four peaks assigned to pyridinic, pyrrolic, graphitic, and pyridine N-oxide species, with the relative ratio of 31, 19, 40, and 9%, respectively. The C 1s peak region in the XPS spectrum (Fig. 1i) was deconvoluted to three peaks at around 284.6 eV, 285.2 eV and 285.7 eV, assigned to C–C/C=C, C–N, and C=N with the relative ratio of 36, 42, and 22%, respectively, further confirming the presence of abundant nitrogen dopants in the carbon network.

The wide XPS survey showed no metal species of detectable quantity. (Fig. S7). The metal-free nature of the NAC catalyst was also validated by inductively coupled plasma mass spectrometry (ICP-MS) analysis (Table S1). Control experiments (Fig. S8) using a metal-free activated carbon and an empty reactor (no catalyst) were performed to confirm that the observed activity originates primarily from the active sites of NAC.

Overall, the characteristics of the NAC catalyst, including high nitrogen content, homogeneous dispersion, large surface area, and ordered mesoporosity, not only provide a high density of accessible active sites but also permit the molecular-level investigation of the structures of active sites and reactive intermediates together with the bond activation mechanism.

Catalytic studies

The direct dehydrogenation of ethylbenzene over the NAC catalyst was carried out in a plug-flow reactor at various temperatures, using a feed rate of 0.4 g_{EB} $g_{cat}^{-1} \cdot h^{-1}$ and a partial pressure of 56 Pa (Fig. 2a and S9). Styrene formation is observed as low as 180 °C, which is a rare occurrence for metal-based or metal-free catalysts.[25,26] Considering the
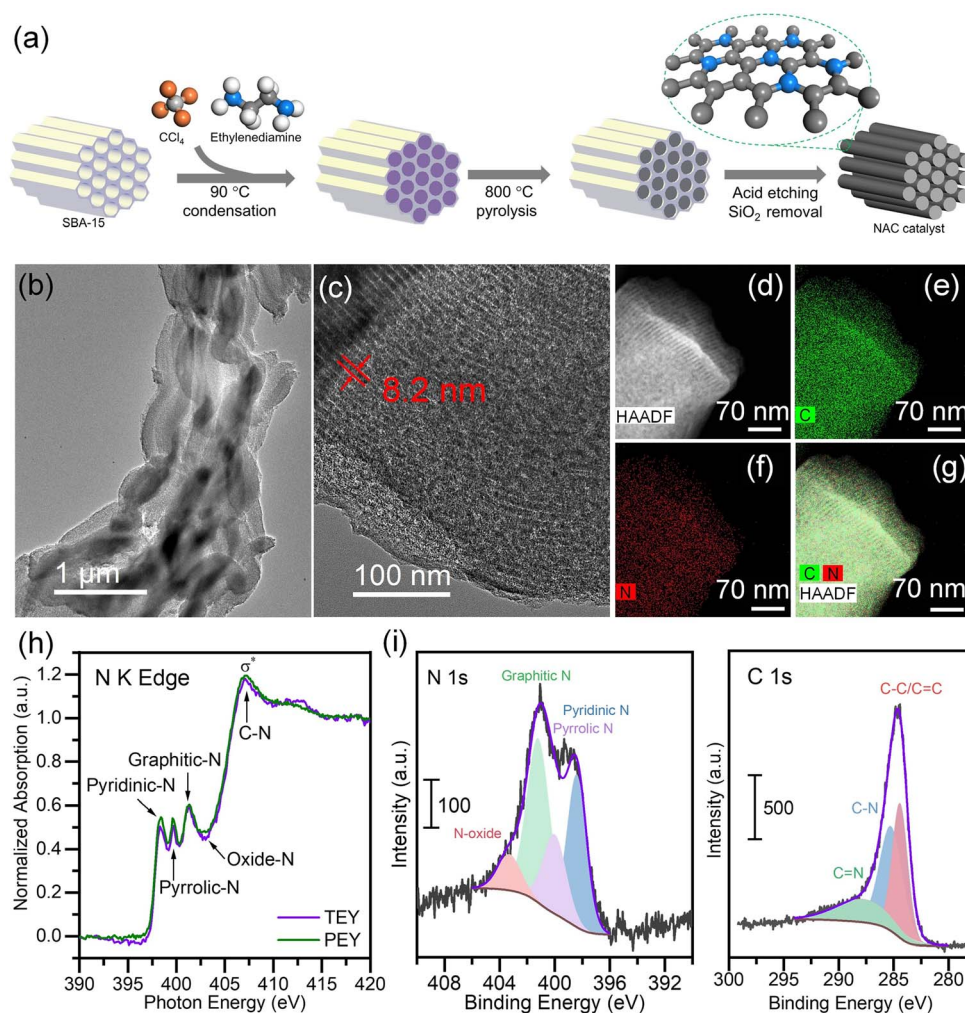
Fig. 1 NAC catalyst synthesis and structural characterization. (a) Scheme of the synthetic method for the NAC catalyst. (b and c) Transmission electron microscopy images of the NAC catalyst. (d–g) Aberration-corrected high-angle annular dark-field scanning transmission electron microscopy (HAADF−STEM) images and energy dispersive spectroscopy (EDS) mapping of the NAC catalyst. Carbon element is presented in green and nitrogen in red in the EDS mapping. (h) Nitrogen K-edge near-edge X-ray absorption fine structure (NEXAFS) spectra of NAC catalyst (TEY refers to total electron yield, a detection mode that is more bulk-sensitive, while PEY refers to partial electron yield, which is more surface-sensitive). (i) N 1s and C 1s X-ray photoelectron spectroscopy (XPS) spectra of the NAC catalyst. Showing pyridinic N (blue), pyrrolic N (purple), graphitic N (green), and pyridine N-oxide (red) in N 1s spectra and C−C/C≡C (red), C−N (blue), and C≡N (green) in C 1s spectra. Intensity is reported in arbitrary units (a.u.).

thermodynamic limitation (equilibrium conversion $\approx$ 1% at 180 °C, Fig. S10), this highlights the NAC catalyst's superior activity, making it a promising candidate for LOHC applications. At 300 °C, a steady-state conversion of 10% was achieved at long contact time (0.07 g_{EB} g_{cat}^{-1} h^{-1}, Fig. S11) and a steady-state reaction rate of 0.2 mmol g^{-1} h^{-1} at short contact time (0.4 g_{EB} g_{cat}^{-1} h^{-1}, Fig. 2a). At 550 °C, reactions at different contact times were investigated (Fig. 2b). The steady-state reaction rate of 6.0 mmol g^{-1} h^{-1} was achieved at the weight hourly space velocity (WHSV) of 8.0 h^{-1} (Fig. S12), ranking it among the top-performing carbon-based metal-free catalysts (1 to 7 mmol g^{-1} h^{-1}, Table S2) reported for the ethylbenzene DDH reaction.[12,22]

Ethylbenzene conversion remained nearly constant at 300 and 400 °C. A similar phenomenon was also observed in a temperature-programmed reaction (TPR) when ethylbenzene

conversion initially rises to 8% at 250 °C, remains steady up to 350 °C, then increases to 40% at 550 °C (Fig. S13). To understand temperature-dependent behavior, the temperature-programmed desorption (TPD) experiment was performed for ethylbenzene and styrene, showing desorption peaks at 274 and 310 °C, respectively (Fig. S14). The higher desorption temperature indicates that stronger chemisorption of product styrene over reactant ethylbenzene, which inhibits the reaction in the temperature range of 300 to 400 °C.

Over a time-on-stream study of 120 h at 550 °C (Fig. 2c), styrene selectivity remained >99%, which demonstrates that the NAC catalyst does not induce typical side reactions common to metal oxide and activated carbon catalysts, such as dealkylation.[14] The conversion initially drops from 40% to 20% in the first 20 h, and then remains stable in the next 100 h. The thermal stability of active sites under reaction-relevant
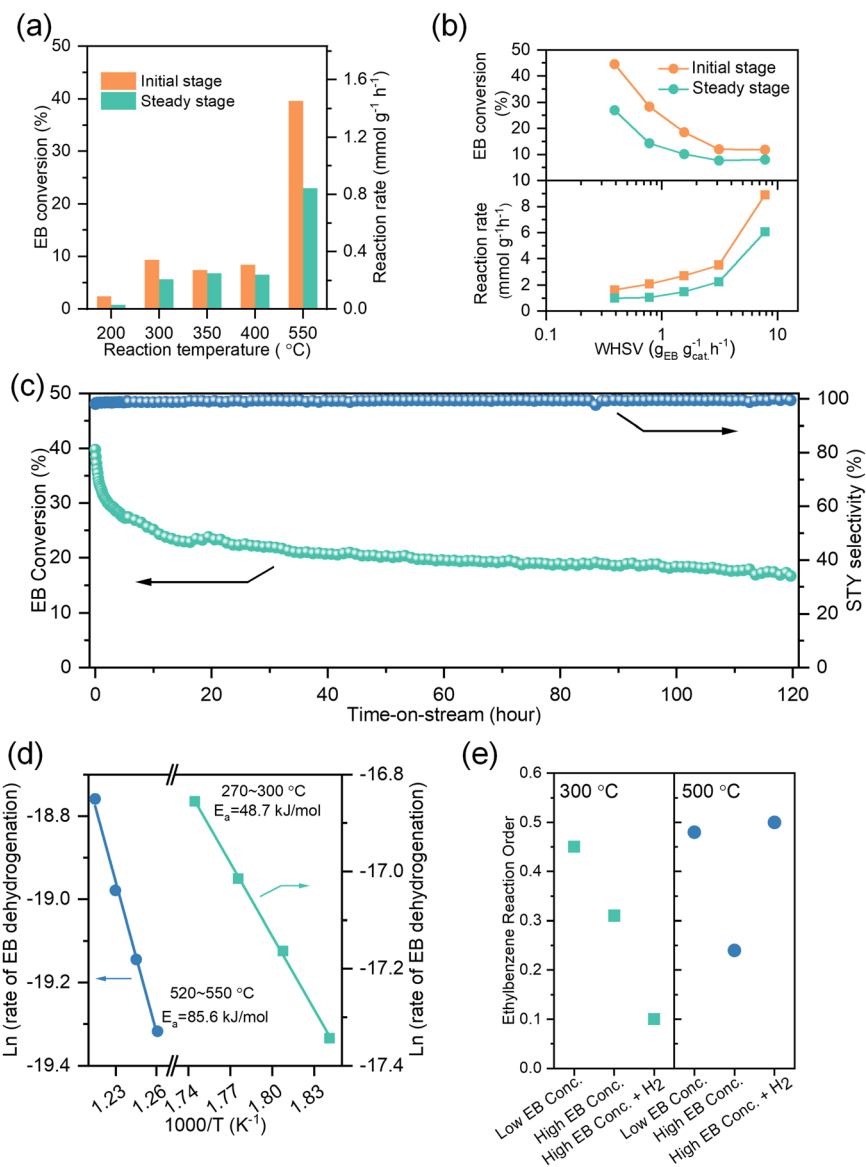
Fig. 2 Catalytic performance for ethylbenzene dehydrogenation over the NAC catalyst. (a) Ethylbenzene dehydrogenation at different reaction temperatures. Conditions: catalyst 20.0 mg, ethylbenzene 56 Pa, WHSV of 0.4 g_{EB} g_{cat}^{-1} h^{-1}, and He 50 mL min^{-1} (STP) at variable temperatures. Initial and steady states were calculated based on results at the time-on-stream of <10 min and 10 h, respectively. (b) Ethylbenzene conversion and reaction rate as a function of WHSV. Conditions: catalyst (1.0 to 20.0) mg, ethylbenzene 56 Pa and WHSV of (0.4 to 8.0) g_{EB} g_{cat}^{-1} h^{-1} at 550 °C. (c) Stability of ethylbenzene dehydrogenation reaction. Conditions: catalyst 20.0 mg, ethylbenzene 56 Pa, WHSV of 0.4 g_{EB} g_{cat}^{-1} h^{-1}, and He 50 mL min^{-1} (STP) at 550 °C. (d) Arrhenius plots for NAC catalyst at (270 to 300) °C and (520 to 550) °C. Conditions: catalyst (10.0 to 20.0) mg, ethylbenzene 56 Pa, ethylbenzene feeding rate of 0.15 μL min^{-1}, and He 50 mL min^{-1} (STP); the ethylbenzene conversion was maintained at levels significantly below equilibrium, less than 10% at high temperatures and below 5% at low temperatures. (e) Effect of temperature, ethylbenzene concentration, and hydrogen on the ethylbenzene reaction orders. Conditions: (10.0 to 20.0) mg catalyst, He 50 mL min^{-1} (STP), H_2 17.5 mL min^{-1} (STP), at 300 or 500 °C. Low and high ethylbenzene concentrations were measured at (0.15 to 1.5) μL min^{-1} and (2.0 to 5.0) μL min^{-1}, respectively. The catalyst was initially allowed to equilibrate for 40 min to 10 h at a given reaction temperature.

conditions is probed by *in situ* ambient-pressure X-ray photoelectron spectroscopy (AP-XPS), conducted from 25 °C to 370 °C in both vacuum and hydrogen atmospheres (Fig. S15). The absence of apparent changes to nitrogen species indicates the robustness of the graphitic nitrogen based active sites under elevated temperature and exposure to H_2. EELS study of the used catalyst after the 120 h reaction (Fig. S16) shows the C K-edge 1s → π* signal (~285 eV, from sp^2 carbon) slightly decreases in relative intensity, while the 1s → σ* peak region

(onset ~290 eV, from both sp^2 and sp^3 carbons) increases. The slight increase of sp^3/sp^2 ratio likely results from the irreversible adsorption of sp^3-rich molecular intermediates onto highly active surface sites in the absence of graphitic coke formation during the reaction, which will lead to enrichment of sp^2 carbon in contrast.

The activation energies were assessed over two different temperature ranges (270 to 300 °C and 520 to 550 °C). As shown in Fig. 2d and S17, the apparent reaction barriers ($E_{a,app}$) are

49 kJ mol^{-1} and 86 kJ mol^{-1}, respectively, suggesting distinct reaction kinetics in these two temperature regimes. Furthermore, we measured the reaction order for ethylbenzene by varying the partial pressure of ethylbenzene at 300 and 500 °C, with and without H$_2$ (Fig. 2e). At 300 °C, the reaction order with respect to ethylbenzene slightly decreases from 0.4 to 0.3 as the partial pressure increases from low (56 to 560 Pa) to high (747 to 1867 Pa) concentrations because of active site saturation by the reactant. When co-feeding 26 kPa H$_2$ at high ethylbenzene coverage, the rate order drops to 0.1. The further decrease in ethylbenzene rate order is likely caused by hydrogen-induced suppression of the net reaction rather than decreased coverage of chemisorbed ethylbenzene, and thus, the reaction becomes less sensitive to the ethylbenzene partial pressure. At 500 °C, the reaction order also decreases from 0.5 to 0.2 as the ethylbenzene partial pressure increases. However, in the presence of 26 kPa H$_2$, the reaction order for ethylbenzene increases to 0.5, suggesting reduced coverage of chemisorbed ethylbenzene by hydrogen at elevated temperatures. A clear understanding of the distinct kinetic behaviors demands molecular-level mechanistic studies of surface intermediates and bond activation.

Mechanistic studies

Isotope labeling experiments are a powerful tool to indirectly identify surface intermediates and their reactivities when direct experimental observation is not possible. Here, we conducted experiments by co-feeding per-deuterated ethylbenzene (C$_8$D$_{10}$) and H$_2$ at variable temperatures (150, 300, 500 and 550 °C) and monitored the effluents using a cascade of offline and online monitoring methods, including off-line solution nuclear magnetic resonance (NMR) spectroscopy (^{1}H and ^{13}C), online gas chromatography with flame ionization detector (GC-FID), and online mass spectroscopy (MS) with the experimental setup illustrated in Fig. S18. Hydrogen/deuterium (H/D) scrambling can occur to both ethylbenzene and styrene because of the reversible chemisorption of all reaction species. H/D distributions in different chemical environments of reaction species can be assigned in ^{1}H and ^{13}C NMR spectra of the gas effluent dissolved in dimethylsulfoxide-d$_6$, based on spectra of authentic samples and literature results.[27,28] GC results showed similar conversions and yields at variable temperatures for deuterated and naturally abundant ethylbenzenes, indicating that reactant deuteration did not significantly influence the catalyst's activity (Fig. S19). In the MS spectra (Fig. 3c and S20), all H/D-exchanged isotopologues exhibit higher intensities as the temperature increases from 300 °C to 500 °C; further increasing the temperature to 550 °C increases the signal intensity for styrenes but not for ethylbenzenes. Under all conditions, H/D exchange only occurs at the aliphatic positions based on NMR and MS results.

At 150 °C, styrene formation was not detected in the ^{1}H NMR spectra, confirming that the conversion was below 1% based on the GC analysis. The partially protonated ethylbenzene signals in the ^{1}H NMR spectra primarily originated from residual protons in the starting C$_8$D$_{10}$ (commercially procured, 97% D).

At 300 °C, the ^{1}H NMR and MS results clearly reveal the formation of H-incorporated styrene isotopologues ($\alpha_1\beta_0$ and $\alpha_1\beta_1$). H/D exchange at the styrene only occurs to β- but not α-position, suggesting that ethylbenzene chemisorption occurs through cleavage of a single C$_\alpha$–H bond, forming intermediate **I1** (Fig. 3d). Interestingly, MS results show the formation of a substantial amount of H-incorporated styrene isotopologues ($\alpha_1\beta_0$ and $\alpha_1\beta_1$; $m/z = 111$ and 110, respectively), suggesting that the rate for C$_\beta$–D activation (k_2) and H/D exchange via intermediate **I2** is fast compared to that for ethylbenzene desorption (k_{-3}) to enable multiple H/D exchange. Despite a high surface coverage of ethylbenzene, the absence of H incorporation into deuterated ethylbenzene by both ^{1}H and ^{13}C NMR (Fig. 3b and S21) suggests that the chemisorption of ethylbenzene is irreversible with a very slow reaction rate for **I1** desorption versus for **I1** formation ($k_{-1} \ll k_1$) while trace MS signals corresponding to ethylbenzene ($m/z = 114$ and 115) is attributed to residual protons in the starting C$_8$D$_{10}$ as well, rather than to newly formed products.

At (500 to 550) °C, in addition to the $\alpha_1\beta_y$ ($y = 0,1$) styrene isotopologues previously observed at 300 °C, protonation at styrene C$_\alpha$ position occurs, as evidenced by the detection of new $\alpha_0\beta_y$ ($y = 0,1$) species shown in the ^{1}H NMR spectra. The formation of styrene-$\alpha_0\beta_y$ can be attributed to three pathways: (1) formation of intermediate **I3** (Fig. S22a) by abstraction of one more C$_\alpha$–H/D from **I1**, (2) reversible styrene chemisorption (Fig. S22b), and (3) reversible ethylbenzene chemisorption (Fig. 3d). While the 1st pathway is ruled out by the significantly higher activation barrier indicated by the theoretical study (discussed in the section below, Fig. 4b), H/D scrambling occurs unselectively to both C$_\alpha$–H and C$_\beta$–H of ethylbenzene in the 2nd pathway but selectively at the C$_\alpha$ position of ethylbenzene in the 3rd pathway (Fig. S22). The ^{13}C NMR spectra can clearly show the extent of deuteration at each carbon due to negligible through-bond coupling (Fig. S21). A much lesser extent of H/D scrambling in ethylbenzene isotopologues ($\alpha_x\beta_y$) observed at C$_\beta$ ($y = 2,3$) versus C$_\alpha$ ($x = 0,1,2$) positions indicates that ethylbenzene chemisorption becomes reversible ($k_{-1} \approx$ or $> k_1$) and ethylbenzene desorption rate (k_{-1}) is faster than that for C$_\beta$–D activation (k_2). As discussed above, the two-slope Arrhenius behavior ($E_a = 49$ kJ mol^{-1} at 300 °C and $E_a = 86$ kJ mol^{-1} at 500–550 °C) supports a temperature-dependent shift in the apparent rate-controlling process. In this scenario, the measured E_a reflects contributions from both the intrinsic surface reaction and temperature-dependent adsorption/coverage terms. Under high-coverage conditions at low temperature, adsorption (and the associated site-blocking effects) dominates the temperature dependence of the observed rate, yielding a lower apparent E_a. At higher temperature, surface coverage decreases and vacant sites are restored, so the intrinsic surface reaction becomes rate limiting and the apparent E_a approaches the true kinetic barrier for dehydrogenation.

In summary, at 300 °C, ethylbenzene dehydrogenation initiates with irreversible cleavage of C$_\alpha$–D to form the surface sorbed intermediate **I1** (chemisorbed ethylbenzene), and **I1** further undergoes multiple C$_\beta$–D bond activations via **I2** prior to
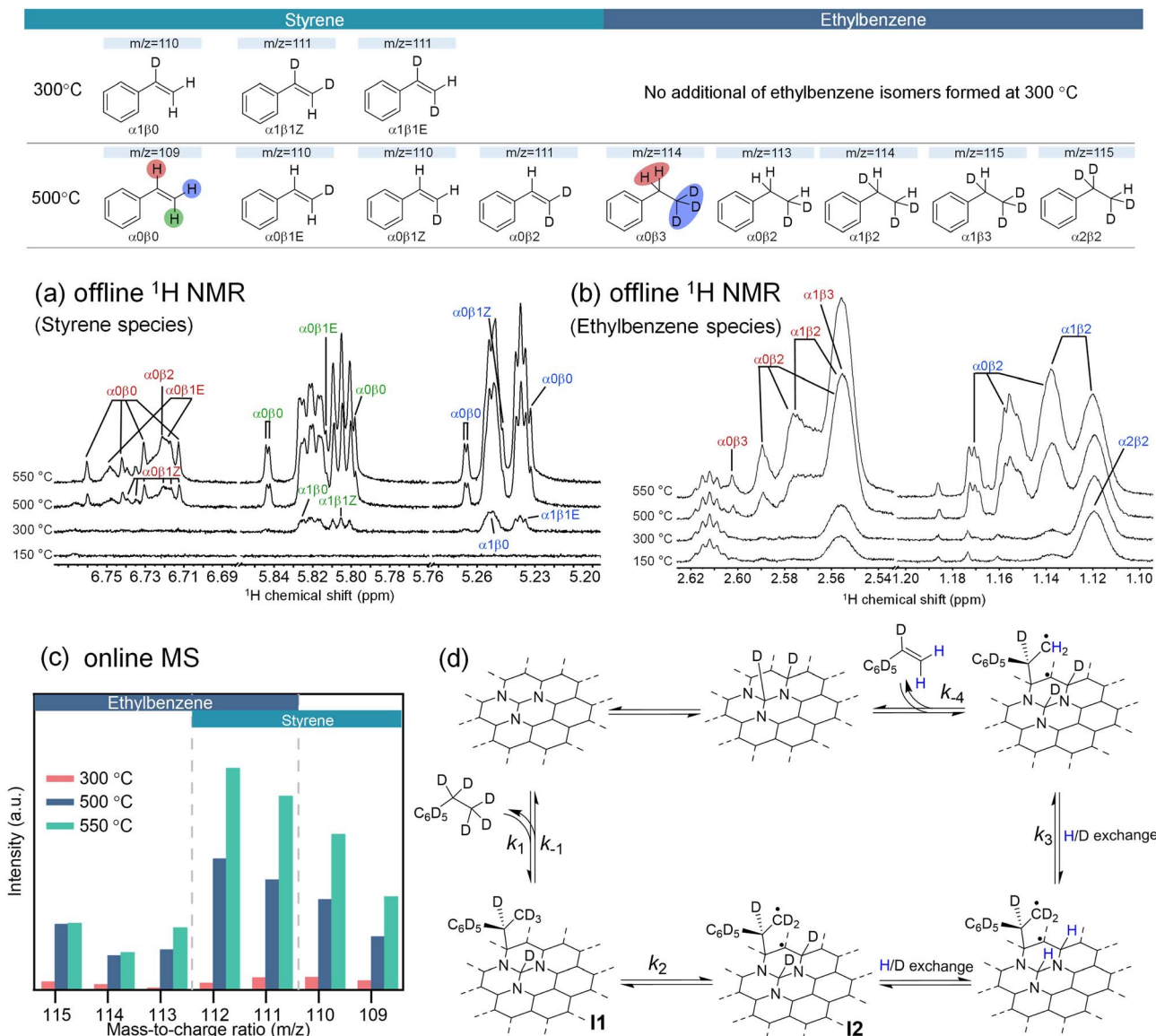
Fig. 3 Identification of reaction pathways for ethylbenzene DDH over NAC catalyst. Isotope labelling experiments with ethylbenzene-d$_{10}$ and hydrogen were performed at variable temperatures, with the effluent analyzed using offline ^{1}H NMR (a and b) and online MS (c) and FID. Conditions: catalyst 20.0 mg, ethylbenzene 56 Pa, WHSV of 0.4 g$_{EB}$ g$_{cat}^{-1} \cdot$h^{-1}, He 32.5 mL min^{-1} (STP), and H2 17.5 mL min^{-1} (STP). The H/D exchanged species are denoted as $\alpha_x\beta_y$, where x and y represent the number of deuterium atoms at the α and β carbons, respectively. Cis- and trans-isomers of partially H/D-exchange styrene are labelled as Z and E, respectively. Intensity is reported in arbitrary units (a.u.). (d) Proposed main reaction pathway.

slow styrene desorption. At 500–550 °C, the ethylbenzene chemisorption is reversible, resulting in more pronounced H/D scrambling at C$_\alpha$ position of ethylbenzene and styrene. The temperature-dependent reversibility of ethylbenzene chemisorption, forming **I1**, is corroborated by H$_2$-induced changes in the ethylbenzene rate order (Fig. 2e).
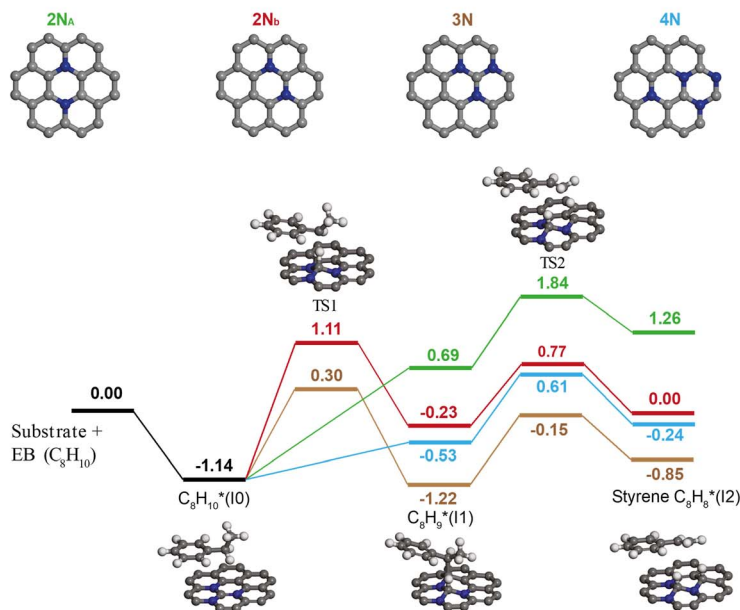
Theoretical studies

Density functional theory (DFT) calculations were performed to gain molecular-level insights into the bond activation mechanism of ethylbenzene dehydrogenation on the NAC catalyst. Our previous DFT study revealed a sharp peak near the Fermi level in

the density of states (DOS), indicating the high reactivity of carbon atoms near nitrogen sites, where desorbed hydrogen preferentially adsorbs.[21] Experimental evidence suggests the presence of two intermediates, **I1** and **I2** (Fig. 3d). Consequently, energy diagrams for ethylbenzene dehydrogenation were constructed on four potential nitrogen assembly sites with 2–4 graphitic nitrogens (Fig. 4a).
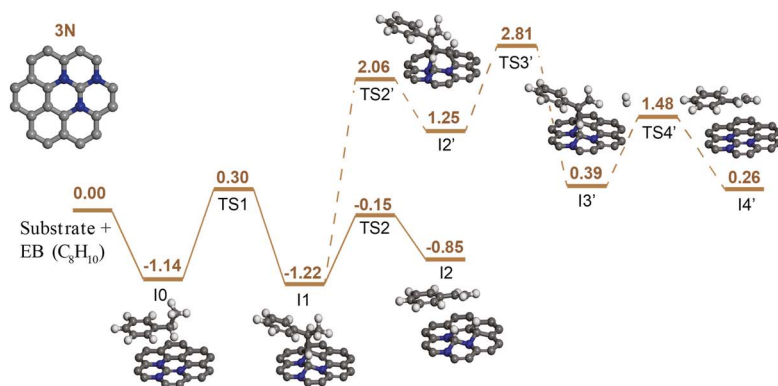
The adsorption energy of ethylbenzene on all four NAC sites is −1.14 eV, indicating strong adsorption that leads to high coverage and reduced reaction order in ethylbenzene. During C$_\alpha$–H cleavage to form intermediate **I1**, the computed intrinsic activation barriers for **2N$_b$** and **3N** are 2.25 eV and 1.44 eV,

Fig. 4 Reaction pathway of ethylbenzene direct dehydrogenation over the NAC catalyst. (a) Energy diagrams for ethylbenzene dehydrogenation to styrene on different NAC substrates. The insets show the calculated structures of reaction intermediates and transition states for the reaction on the **3N** configuration. (b) Energy diagram of ethylbenzene dehydrogenation on the **3N** configuration. The solid line represents the low-temperature reaction route as shown in Fig. 3d and 4a, while the dashed line represents the pathway where intermediate **I1** undergoes second C_α–H bond cleavage and further dehydrogenation/hydrogenation to form styrene. "I" denotes the intermediate, and "TS" denotes the transition state. Note: to reduce computational costs, the substrate is assumed to be pristine, and the hydrogen at the middle C is involved in the second step. The NAC model used in our DFT calculations is an idealized representation introduced to probe the local catalytic role of graphitic N configurations, and therefore it should not be interpreted as reflecting the exact nitrogen-to-carbon ratio or the precise distribution of N species in the experimental NAC catalysts.

respectively, whereas for **2N$_a$** and **4N**, this step proceeds barrier-free with reaction energies of 1.83 eV and 0.61 eV, respectively. The second step, C_β–H cleavage to form styrene, exhibits very comparable intrinsic activation barriers among all different nitrogen configurations (1.07 eV for **3N**). These findings suggest that the investigated configurations with 2–4 closely-spaced graphitic nitrogens show low activation barriers for ethylbenzene dehydrogenation, in particular with **3N**, which demonstrates the highest catalytic activity because of the enhanced stability of the partially dehydrogenated ethylbenzene. The calculated activation energy for ethylbenzene dehydrogenation on **3N** is lower than on iron oxide catalysts (*ca.* 1.69 eV),[29] corroborating the superior performance of the NAC catalyst at mild reaction conditions.

In addition, we also considered another reaction path on **I1**, involving the cleavage of a second C_α–H to form intermediate **I3** (labelled as **I3′** in Fig. 4b). This path was calculated using the most active **3N** substrate, illustrated as a dashed line in Fig. 4b.

Apparent barriers for the additional C_α–H and C_β–H cleavage to form I2′ and I3′ (2.06 eV and 2.81 eV, respectively) are significantly higher than the formation of physiosorbed styrene (I2, −0.15 eV), suggesting these additional C–H activation steps of I1 are energy-prohibitive. By ruling out other potential C–H activation steps, we refine the hypothesis for the observed H/D scrambling at the styrene C_α position only at 500–550 °C to the reversible ethylbenzene chemisorption pathway (Fig. 3d), which is further evidenced by similar energy barriers for the interconversion of the physiosorbed and chemisorbed ethylbenzene (I0 and I1, respectively).

Substrate scope study of dehydrogenation

To further demonstrate the versatility of the NAC catalyst, we explored its catalytic performance on the DDH reactions of three other alkanes (cyclohexane, decalin, and tetralin) as promising LOHCs. The NAC catalyst effectively catalyzed C–H bond activation of all three six-membered ring LOHCs at 550 °C (Table 1 and Fig. S23), typically requiring transition metal ensembles.[10,30] For cyclohexane, 34% conversion was achieved with 85% selectivity for cyclohexene and 15% for benzene. As for decalin, the conversion was 35%, with selectivities over 88% and 12% for tetralin and naphthalene, respectively. For tetralin, 40% conversion was observed with 97% selectivity towards naphthalene. These results highlight the alkane DDH activity of NAC catalysts comparable to transition metal-based catalysts.

Reversible hydrogen storage

A process using the same catalyst to achieve both dehydrogenation and rehydrogenation has unique techno–economic benefits for reversible hydrogen storage. Thus, for a proof of concept, the same NAC catalyst was evaluated for the rehydrogenation of styrene to ethylbenzene. The NAC catalyst converts styrene to ethylbenzene with 100% selectivity and ca. 45% conversion at a feeding rate of $0.21\,g_{styrene}\,g_{cat.}^{-1}\,h^{-1}$ at 250 °C (Fig. S24). The fact that NAC can catalyze both the hydrogenation and dehydrogenation reactions makes it possible to use a single catalyst to perform reversible hydrogen storage at a moderate temperature (250 °C, Fig. S25).

Conclusions

In this work, we demonstrate a highly effective metal-free nitrogen assembly carbon (NAC) catalyst for direct dehydrogenation (DDH) of alkanes (ethylbenzene, cyclohexane, decalin, and tetralin), exhibiting superior activity and selectivity. Notably, the catalyst is also capable of efficiently hydrogenating styrene back to ethylbenzene at 250 °C, demonstrating its potential for reversible hydrogen storage using a single, metal-free catalytic system. AP-XPS characterization confirmed the stability of nitrogen species for DDH across the temperature range and DFT calculations revealed that carbon atoms near closely spaced graphitic nitrogen sites are critical for hydrogen and C–H bond activation. The apparent reaction barriers differ at low ($\approx$300 °C) and high temperatures ($\geq$500 °C), which can be explained by changes to the reversibility of surface reactions elucidated by isotope labeling experiments and cascade reaction monitoring. This work advances the molecular-level understanding of surface sites, bond activation mechanism, and reaction kinetics of metal-free carbocatalysts in direct dehydrogenation reactions, offering valuable insights into prospective design of catalysts alternative to precious metals for reversible hydrogen storage.

Author contributions

W. H., L. Q., and B. W. conceived of and supervised the project. J. Z. and R. K. B. conducted most of the catalytic reactions and performed the basic characterizations of the catalysts. V. T. N. and B. W. performed the DFT calculations. J. D. J., K. P. R., J. M., C. J., and S. D. S. carried out and analyzed the X-ray-based characterizations (AP-XPS and NEAXFS). J. O. and L. Z. conducted the electron microscopy studies. Z. L. and C. M. acquired additional catalysis and characterization data, as suggested by reviewers during the revision. J. Z., R. K. B., and L. Q. wrote the original draft. J. D. J., S. D. S., B. W., L. Q., and W. H. provided scientific guidance and critical discussion. All authors contributed to discussions and revisions of the manuscript.

Conflicts of interest

There are no conflicts to declare.

Data availability

The data supporting this article have been included as part of the supplementary information (SI). Supplementary information: experimental procedures, catalyst characterizations, catalytic data, and reaction pathways. See DOI: https://doi.org/10.1039/d5sc08580b.

Table 1 Substrate scope study for LOHCs dehydrogenation[a]

Entry	LOHC	Conv. (%)	Product	Selec. (%)
1	(cyclohexane)	33.8	(cyclohexene)	85.0
			(benzene)	15.0
2	(decalin)	35.1	(tetralin)	87.9
			(naphthalene)	12.1
3	(tetralin)	39.9	(naphthalene)	97.2

[a] Reaction conditions: 10.0 mg catalyst, 550 °C temperature, 5 mL min⁻¹. He through a saturator for alkane substrates, and a total He flow rate of 50 mL min⁻¹.

Acknowledgements

References

1 P. Schwach, X. Pan and X. Bao, Direct Conversion of Methane to Value-Added Chemicals over Heterogeneous Catalysts: Challenges and Prospects, *Chem. Rev.*, 2017, **117**, 8497–8520.

2 Y. Dai, X. Gao, Q. Wang, X. Wan, C. Zhou and Y. Yang, Recent progress in heterogeneous metal and metal oxide catalysts for direct dehydrogenation of ethane and propane, *Chem. Soc. Rev.*, 2021, **50**, 5590–5630.

3 P. Preuster, C. Papp and P. Wasserscheid, Liquid Organic Hydrogen Carriers (LOHCs): Toward a Hydrogen-free Hydrogen Economy, *Acc. Chem. Res.*, 2017, **50**, 74–85.

4 Y. He, Y. Song, D. A. Cullen and S. Laursen, Selective and Stable Non-Noble-Metal Intermetallic Compound Catalyst for the Direct Dehydrogenation of Propane to Propylene, *J. Am. Chem. Soc.*, 2018, **140**, 14010–14014.

5 F. Huang, M. Peng, Y. Chen, Z. Gao, X. Cai, J. Xie, D. Xiao, L. Jin, G. Wang, X. Wen, N. Wang, W. Zhou, H. Liu and D. Ma, Insight into the Activity of Atomically Dispersed Cu Catalysts for Semihydrogenation of Acetylene: Impact of Coordination Environments, *ACS Catal.*, 2022, **12**, 48–57.

6 C. Li and G. Wang, Dehydrogenation of light alkanes to mono-olefins, *Chem. Soc. Rev.*, 2021, **50**, 4359–4381.

7 J. Diao, M. Hu, Z. Lian, Z. Li, H. Zhang, F. Huang, B. Li, X. Wang, D. S. Su and H. Liu, Ti3C2Tx MXene Catalyzed Ethylbenzene Dehydrogenation: Active Sites and Mechanism Exploration from both Experimental and Theoretical Aspects, *ACS Catal.*, 2018, **8**, 10051–10057.

8 M. Peng, Z. Jia, Z. Gao, M. Xu, D. Cheng, M. Wang, C. Li, L. Wang, X. Cai, Z. Jiang, H. Jiang, N. Wang, D. Xiao, H. Liu and D. Ma, Antisintering Pd1 Catalyst for Propane Direct Dehydrogenation with *In Situ* Active Sites Regeneration Ability, *ACS Catal.*, 2022, **12**, 2244–2252.

9 S. Ramadhani, Q. N. Dao, Y. Imanuel, M. Ridwan, H. Sohn, H. Jeong, K. Kim, C. W. Yoon, K. H. Song and Y. Kim, Advances in Catalytic Hydrogenation of Liquid Organic Hydrogen Carriers (LOHCs) Using High-Purity and Low-Purity Hydrogen, *ChemCatChem*, 2024, **16**, e202401278.

10 L. Chen, P. Verma, K. Hou, Z. Qi, S. Zhang, Y.-S. Liu, J. Guo, V. Stavila, M. D. Allendorf, L. Zheng, M. Salmeron, D. Prendergast, G. A. Somorjai and J. Su, Reversible dehydrogenation and rehydrogenation of cyclohexane and methylcyclohexane by single-site platinum catalyst, *Nat. Commun.*, 2022, **13**, 1092.

11 J. Sheng, B. Yan, W.-D. Lu, B. Qiu, X.-Q. Gao, D. Wang and A.-H. Lu, Oxidative dehydrogenation of light alkanes to olefins on metal-free catalysts, *Chem. Soc. Rev.*, 2021, **50**, 1438–1468.

12 J. Shi, Y. Wei, D. Zhou, L. Zhang, X. Yang, Z. Miao, H. Qi, S. Zhang, A. Li, X. Liu, W. Yan, Z. Jiang, A. Wang and T. Zhang, Introducing Co–O Moiety to Co–N–C Single-Atom Catalyst for Ethylbenzene Dehydrogenation, *ACS Catal.*, 2022, **12**, 7760–7772.

13 W. Qi and D. Su, Metal-Free Carbon Catalysts for Oxidative Dehydrogenation Reactions, *ACS Catal.*, 2014, **4**, 3212–3218.

14 J. Zhang, D. S. Su, R. Blume, R. Schlögl, R. Wang, X. Yang and A. Gajović, Surface Chemistry and Catalytic Reactivity of a Nanodiamond in the Steam-Free Dehydrogenation of Ethylbenzene, *Angew. Chem., Int. Ed.*, 2010, **49**, 8640–8644.

15 L. Cao, P. Dai, L. Zhu, L. Yan, R. Chen, D. Liu, X. Gu, L. Li, Q. Xue and X. Zhao, Graphitic carbon nitride catalyzes selective oxidative dehydrogenation of propane, *Appl. Catal. B Environ.*, 2020, **262**, 118277.

16 K. Sun, H. Shan, R. Ma, P. Wang, H. Neumann, G.-P. Lu and M. Beller, Catalytic oxidative dehydrogenation of N-heterocycles with nitrogen/phosphorus co-doped porous carbon materials, *Chem. Sci.*, 2022, **13**, 6865–6872.

17 F. Guo, P. Yang, Z. Pan, X.-N. Cao, Z. Xie and X. Wang, Carbon-Doped BN Nanosheets for the Oxidative Dehydrogenation of Ethylbenzene, *Angew. Chem., Int. Ed.*, 2017, **56**, 8231–8235.

18 H. Hu, Y. Nie, Y. Tao, W. Huang, L. Qi and R. Nie, Metal-free carbocatalyst for room temperature acceptorless dehydrogenation of N-heterocycles, *Sci. Adv.*, 2022, **8**, eabl9478.

19 Z. Luo, Z. Yin, J. Yu, Y. Yan, B. Hu, R. Nie, A. F. Kolln, X. Wu, R. K. Behera, M. Chen, L. Zhou, F. Liu, B. Wang, W. Huang, S. Zhang and L. Qi, General Synthetic Strategy to Ordered Mesoporous Carbon Catalysts with Single-Atom Metal Sites for Electrochemical CO2 Reduction, *Small*, 2022, **18**, 2107799.

20 Z. Luo, L. Li, V. T. Nguyen, U. Kanbur, Y. Li, J. Zhang, R. Nie, A. Biswas, S. L. Bud'ko, J. Oh, L. Zhou, W. Huang,

A. D. Sadow, B. Wang, S. L. Scott and L. Qi, Catalytic Hydrogenolysis by Atomically Dispersed Iron Sites Embedded in Chemically and Redox Non-innocent N-Doped Carbon, *J. Am. Chem. Soc.*, 2024, **146**, 8618–8629.

21 Z. Luo, R. Nie, V. T. Nguyen, A. Biswas, R. K. Behera, X. Wu, T. Kobayashi, A. Sadow, B. Wang, W. Huang and L. Qi, Transition metal-like carbocatalyst, *Nat. Commun.*, 2020, **11**, 4091.

22 Z. Zhao, Y. Dai, J. Lin and G. Wang, Highly-Ordered Mesoporous Carbon Nitride with Ultrahigh Surface Area and Pore Volume as a Superior Dehydrogenation Catalyst, *Chem. Mater.*, 2014, **26**, 3151–3161.

23 D. A. Bulushev, M. Zacharska, E. V. Shlyakhova, A. L. Chuvilin, Y. Guo, S. Beloshapkin, A. V. Okotrub and L. G. Bulusheva, Single Isolated Pd2+ Cations Supported on N-Doped Carbon as Active Sites for Hydrogen Production from Formic Acid Decomposition, *ACS Catal.*, 2016, **6**, 681–691.

24 D. E. Starr, in *Ambient Pressure Spectroscopy in Complex Chemical Environments*, American Chemical Society, 2021, vol. 1396, pp. 1–17.

25 L. Wang, J. Diao, M. Peng, Y. Chen, X. Cai, Y. Deng, F. Huang, X. Qin, D. Xiao, Z. Jiang, N. Wang, T. Sun, X. Wen, H. Liu and D. Ma, Cooperative Sites in Fully Exposed Pd Clusters for Low-Temperature Direct Dehydrogenation Reaction, *ACS Catal.*, 2021, **11**, 11469–11477.

26 K. Zhang, G. Cui, M. Yuan, H. Huang, N. Li, J. Xu, G. Wang and C. Li, Sn-decorated CeO2 with different morphologies for direct dehydrogenation of ethylbenzene, *J. Rare Earths*, 2024, **42**, 102–109.

27 H. Nies, H. Bauer, K. Roth and D. Rewicki, The complete 1H spectral analysis of styrene, *J. Magn. Reson.*, 1969, **1980**(39), 521–524.

28 T. Schaefer, G. H. Penner and R. Sebastian, 1H nuclear magnetic resonance and molecular orbital studies of the structure and internal rotations in ethylbenzene, *Can. J. Chem.*, 1987, **65**, 873–877.

29 K. Coulter, D. W. Goodman and R. G. Moore, Kinetics of the dehydrogenation of ethylbenzene to styrene over unpromoted and K-promoted model iron oxide catalysts, *Catal. Lett.*, 1995, **31**, 1–8.

30 Y. Deng, Y. Guo, Z. Jia, J.-C. Liu, J. Guo, X. Cai, C. Dong, M. Wang, C. Li, J. Diao, Z. Jiang, J. Xie, N. Wang, H. Xiao, B. Xu, H. Zhang, H. Liu, J. Li and D. Ma, Few-Atom Pt Ensembles Enable Efficient Catalytic Cyclohexane Dehydrogenation for Hydrogen Production, *J. Am. Chem. Soc.*, 2022, **144**, 3535–3542.